



Gentle way to build reduced titanium dioxide nanodots integrated with graphite-like carbon spheres: From DFT calculation to experimental measurement

Zhifeng Jiang^{a,b,c,*}, Weiming Wan^b, Wei Wei^a, Kangmin Chen^a, Huaming Li^a,
Po Keung Wong^{c,*}, Jimin Xie^a

^a Institute for Energy Research, School of Chemistry and Chemical Engineering, Analysis and Test Center, Jiangsu University, Zhenjiang, Jiangsu, 212013, PR China

^b Department of Chemical Engineering, Columbia University, New York, NY, 10027, United States

^c School of Life Sciences, The Chinese University of Hong Kong, Shatin, NT, Hong Kong SAR, PR China

ARTICLE INFO

Article history:

Received 24 August 2016

Received in revised form 5 November 2016

Accepted 21 November 2016

Available online 22 November 2016

Keywords:

Reduced TiO₂

Photocatalysis

Degradation

H₂-production

DFT calculation

ABSTRACT

Extending the ultraviolet response of anatase TiO₂ into visible light range and effectively decreasing the recombination rate of photo-generated carriers are vital to promote the practical applications in the fields of hydrogen generation and water pollutant treatment of TiO₂-based photocatalysts. Here we present a mild way to build composite of partial reduced TiO₂ nanodots coated graphite-like carbon spheres (g-CS@TiO_{2-x}) via a green solvothermal approach with relative low temperature. The chemical structure and electronic property of 3D g-CS@TiO_{2-x} composites have been investigated by DFT. Our DFT calculation results indicates that some mid-levels are formed between the CB and VB of TiO_{2-x}, which is beneficial to its visible absorption ability. The calculation results also show that bridge of Ti—O—C formed between g-CS and TiO_{2-x} may let the composite possesses superior charge separation property. The experimental results demonstrate that the obtained 3D g-CS@TiO_{2-x} can serve as an effective visible-light-driven photocatalyst for hydrogen production and organic pollutants degradation. The good visible light absorption introduced by Ti³⁺ and 3D g-CS, the well-known electron transfer capability of g-CS, the matched electron structures of TiO_{2-x} and g-CS, and perfect interface between TiO_{2-x} and g-CS (Ti—O—C bridge), efficiently boost visible light photocatalytic performance via one-level electron transfer process.

© 2016 Elsevier B.V. All rights reserved.

1. Introduction

Anatase titanium dioxide (TiO₂), which has promising energy and environmental applications, is the most frequently used photocatalyst owing to its low cost, high stability, and excellent recyclability [1,2]. Nevertheless, two main drawbacks have greatly limited the widespread use of TiO₂: (1) due to the large band gap (3.2 eV for anatase), its optical absorption is confined to the UV region of the solar spectrum, which makes up only 3–5% of the solar spectrum; (2) high recombination rate of photo-induced charge carriers [3,4]. Quantum yield (Φ), which is defined as the number of events occurring per photon absorbed, is often used to evaluate the photocatalytic efficiency of as-prepared photocatalysts. Φ

is proportional to a simple relationship like, $\Phi \propto k_{ct}/(k_{ct} + k_r)$, where k_{ct} is the rate of the charge transfer processes and k_r indicates the electron hole recombination rate. According to this equation, it is important to increase the separation rate of electron-hole under illumination in order to improve the quantum yield [5]. To this end, many investigations have been attempted to shift the optical response of TiO₂ from UV to visible light region to harvest solar energy more efficiently, and to decrease the recombination efficiency of charge carrier pairs.

For the first issue, various approaches have been performed to make anatase TiO₂ sensitive to visible light [6], and most of them are concerned on incorporating dopants at the O and/or Ti sites to introduce mid-gap states into the TiO₂ band gap [7]. As a result, the white color of TiO₂ might change, giving a clear sign that visible light has been absorbed [8]. Nevertheless, impurity incorporation can result in thermal instability and increasing carrier recombination centers. Moreover, the need for an expensive ion-implantation facility poses significant limitation for this strategy. Reduced TiO₂ (TiO_{2-x}), which

* Corresponding authors

E-mail addresses: ntjiangzf@sina.com (Z. Jiang), pkwong@cuhk.edu.hk (P.K. Wong).

contains self-doped Ti^{3+} ions, has been demonstrated the absorption in visible light and attract a great interest in recent years [9–12]. Chen et al. obtained black TiO_2 nanoparticles with 1.0 eV bandgap through high-pressure hydrogenation of crystalline TiO_2 , and a great improvement of photocatalytic hydrogenation was obtained [9]. Since then, a variety of methods for the synthesis of black TiO_2 have been developed, which truly represent a big breakthrough in the photocatalytic performance [13–16]. However, most of the reported methods, including heating TiO_2 under vacuum or reducing conditions with high temperature, chemical vapor deposition and high energy particle bombardment, have multiple steps, harsh synthesis condition and/or uneconomical facilities, which makes them difficult to implement for practical use [17,18]. Additionally, throughout these prepared reduced TiO_2 nanoparticles (NPs), agglomeration has been deemed as another critical problem that can't be ignored [19–22]. Therefore, developing an economical and facile method for fabricating a stable, well-dispersive, reduced TiO_2 in a mild environment remains a great challenge.

To overcome the second problem, works concerning on modifying TiO_2 with some electron acceptors (e.g., noble NPs, carbon-based materials) were widely investigated [22–32]. It is not appropriate for large scale application due to the high cost of noble metal NPs. Therefore, low-cost additives of carbon-based materials may become effective alternatives to replace rare noble metal. Previous reports indicated that hybrid materials of TiO_2 and carbon, including activated carbon, carbon nanotubes, graphene and fullerenes (C_{60}), are able to show improved photocatalytic activity than bare TiO_2 [33–36]. However, report focused on reduced TiO_2 /carbon based composites is seldomly been investigated. In addition, while electrons transfer from TiO_{2-x} to carbon is clearly important, however, the electron transfer channels are still lacking of theoretical research. Moreover, it is not very clear whether the introduction of carbon-based material will change the band structure of TiO_{2-x} .

Herein, we present a gentle way to construct partial reduced TiO_2 nanodots integrated with graphite-like carbon spheres (g-CS@ TiO_{2-x}). The composites can be prepared *via* a green solvothermal approach with relative low temperature (200 °C). The as-prepared composite can efficiently overcome the drawbacks mentioned-above to some extent. Firstly, the introduction of Ti^{3+} state would change the TiO_2 electronic structure (narrow the bandgap), thus, $\text{Ti}^{3+}/\text{TiO}_2$ can absorb visible light. Moreover, the addition of graphite-like carbon spheres (g-CS) could increase light absorption, and thus enhanced photocatalytic activity. Secondly, the excited electrons would transfer from the conduction band of TiO_{2-x} to g-CS as g-CS redox potential is less negative than the conduction band edge of TiO_2 as well as the excellent electron transport property of g-CS. The interfacial transfer of photogenerated electrons between TiO_{2-x} and g-CS can lead to the effective charge separation. Additionally, with this method, TiO_2 nanodots can be uniformly deposited on the surface of g-CS without aggregation. To investigate the effect of Ti^{3+} and g-CS on the physicochemical properties, we have modeled, optimized, and studied the electronic properties of TiO_2 , TiO_{2-x} , and g-CS@ TiO_{2-x} by means of DFT based calculations. Our DFT results indicated that a miniband rising up closely below the conducting band minimum (CBM) after introducing Ti^{3+} into TiO_2 , which is responsible for band gap narrowing. Additionally, the DFT calculation is employed to investigate charge transfer actions between 3D g-CS and anatase TiO_{2-x} . The excellent mobility of electrons is expected to be able to increase the separation rate of excited charge carriers due to the formation of chemical bond (Ti–O–C bridge) between 3D g-CS and TiO_{2-x} . These results can be ascribed to some mid-gap energy levels localized between the valence band maximum (VBM) and conduction band-minimum (CBM), resulting in the electron transfer from VBM to a mid-gap energy level or from a mid-gap energy level to CBM more

easily. Simultaneously, with these mid-gap levels, the electrons can't easily go back from CB to VBM, which prevents the corresponding recombination. To test the actual photocatalytic activity, the hydrogen generation ability, degradation efficiency, and photoelectrochemical properties of as-prepared photocatalysts are extensively investigated and characterized. It could be found that 3D g-CS@ TiO_{2-x} composites showed the enhanced photocatalytic activity due to the low recombination rate of photogenerated carriers as well as the high light absorption ability. Based on the experimental results, the possible photocatalytic mechanism and photostability of the as-prepared composites are also investigated. Our work present here, can bridge the understanding of theory (DFT) and practical use (photocatalysis in the field of energy and environment) in building TiO_2 -based catalysts.

2. Experimental section

2.1. Materials

Absolute ethanol ($\text{C}_2\text{H}_5\text{OH}$), Tetrabutyl titanate (TBOT), glucose, rhodamine B (RhB) and methylene blue (MB) are of analytical grade and obtained from Sinopharm Chemical Reagent Co., LTD. 4-chlorophenol (4-CP) and ciprofloxacin (CIP) were bought from Aladdin Reagent Co., LTD. All chemicals were of analytical grade and used as purchased without further purification. Deionized water was used for all experiments.

2.2. Preparation of graphite-like carbon spheres (g-CS)

The as-synthesized graphite-like carbon spheres were prepared as follows: In a typical experiment, glucose (0.6 mol/L) was transferred into a Teflon-lined autoclave with a capacity of 50 mL. The autoclave was heated for hydrothermal reaction at 180 °C for 5 h and then cooled naturally to room temperature naturally. The products were separated from the aqueous solution by centrifugation and washed with absolute ethanol for 6 times and dried in a vacuum oven at a temperature of 60 °C overnight to remove the absolute ethanol for the subsequent use and characterizations.

2.3. Fabrication of partial reduced titanium dioxide nanodots integrated with graphite-like carbon spheres (g-CS@ TiO_{2-x})

A typical synthesis of g-CS@ TiO_{2-x} composites were shown in the following steps. Firstly, 4 mL of TBOT were added into $\text{C}_2\text{H}_5\text{OH}$ (40 mL) under stirring, and then the mixture was stirred and ultrasonicated for 1 h. Secondly, 0.2 g of g-CS were dispersed in a mixture of 40 mL absolute ethanol and 0.1 mL deionized water to form a black homogeneous suspension. After that, the mixed solution consisted of 4 mL TBOT and 40 mL $\text{C}_2\text{H}_5\text{OH}$ was injected into the above black suspension under a rate of 1.0 mL min^{-1} . Subsequently, the above suspension was transferred into a Teflon-lined autoclave with a capacity of 100 mL. The autoclave was then heated at 200 °C for 10 h and cooled down to room temperature. Subsequently, the as-prepared samples were separated from the aqueous solution by centrifugation and washed with absolute ethanol for 3 times and dried in a vacuum oven at a temperature of 60 °C overnight to remove the absolute ethanol for the subsequent use and characterizations. For comparison, partial reduced TiO_2 (TiO_{2-x}) nanoparticles are prepared according to the previous report [21].

2.4. DFT calculations

In our theoretical calculations, calculations were performed using the Vienna Ab-initio Simulation Package (VASP) [37], which uses a plane wave basis set with pseudopotentials to represent

core electrons. All calculations in this work were performed in spin unrestricted manner. Electron-ion interactions were treated by the projector augmented wave (PAW) method [4]. The exchange and correlation energy was described using the generalized gradient approximation with the Perdew-Burke-Ernzerhof (PBE) functional [38]. For geometry relaxation, the cutoff energy of 380 eV and a $4 \times 4 \times 2$ Monkhorst–Pack K-points were adopted, which were tested to be enough for both total energy in the systems. To correct the on-site electron correlation, DFT plus Hubbard model (DFT + U) was employed with $U = 4.0$ eV. Graphene layer was used to simulate the g-CS. The atomic position was optimized through PBE calculations with a criterion that required the calculated forces less than 1×10^{-2} eV/Å. The TiO_2 (001) surface was modeled by a three layer 2×6 unit cell. A vacuum layer of 20 Å thick was applied perpendicular to the slab to avoid artificial interactions between the slab and its periodic images.

2.5. Characterization

The crystal structure and phase purity of the prepared samples were analysed by X-ray diffraction (XRD) using D8 Advance X-ray diffractometer (Bruker axis company, Germany) equipped with $\text{Cu-K}\alpha$ radiation ($\lambda = 1.5406$ Å), employing a scanning rate of $0.02^\circ \text{ s}^{-1}$ in the 2θ range from 20 to 80° . Scanning electron microscopy (SEM) was performed on a scanning electron microscope (Hitachi S-4800 II, Japan) operated at an acceleration voltage of 10 kV to characterize the morphologies and the compositions of the prepared samples. Furthermore, the morphology and particle size of the products were also examined by transmission electron microscopy (TEM) which was recorded on a JEOL-JEM-2010 (JEOL, Japan) operating at 200 kV. Ultraviolet–visible (UV–vis) spectroscopy measurements were performed on a UV-2450 ultraviolet–visible spectrophotometer. Raman scattering was obtained at room temperature by a Thermo Electron Corporation DXR Raman spectrometer (USA) using a 532 nm laser source. A Nicolet NEXUS470 FTIR spectrometer was applied to obtain Fourier transform infrared spectra. X-ray photoelectron spectroscopy (XPS) analysis was measured on an ESCALAB MK X-ray photoelectron spectrometer. The excitation light employed in recording fluorescence spectra was 362 nm. The PL spectra of the samples were obtained by a QuantaMaster & TimeMaster Spectrofluorometer (QuantaMasterTM40, USA). The electron spin resonance (ESR) analysis was conducted with an electron paramagnetic resonance A300-10/12 spectrometer (Bruker AXS Company, Germany). Photocurrent measurements and electrochemical impedance spectroscopy (EIS) were performed on CHI 760B electrochemical analyzer (Chenhua Instruments Company, China).

2.6. Photoelectrochemical measurements

Photocurrent measurements were performed in three-electrode quartz cells with a 0.1 M phosphate buffered saline electrolyte solution with platinum wire as the counter electrode, and saturated calomel electrodes (SCE) as the reference electrodes, respectively. The prepared sample film electrodes on ITO were served as the working electrode with an active area of *ca.* 0.5 cm^2 . Working electrodes were prepared as follows: 2.0 mg/mL ($6 \mu\text{L}$) catalysts aqueous solution was spread on the pretreated ITO ($0.5 \text{ cm} \times 1 \text{ cm}$), and dried in air at room temperature to form photocatalysts modified ITO. Electrochemical impedance spectroscopy (EIS) measurements were determined at an AC voltage magnitude of 5 mV with the frequency range of 10^5 – 10^{-1} Hz. A 500W Xe arc lamp was utilized as the light source in the photoelectrochemical measurements.

2.7. H_2 evolution and hazardous pollutant degradation (RhB, MB, CIP, and 4-CP) performances

Hydrogen production experiments were carried out in a 100 mL Pyrex flask connected to a closed gas circulation and evacuation system. Low power UV-LEDs ($3 \times 4 \text{ W}$, 420 nm) (Shenzhen LAMPLIC Science Co. Ltd. China), used as light sources to trigger the photocatalytic reaction, were positioned 1 cm away from the reactor in four different directions. The illumination intensity at the catalyst surface is 60.0 mW. Typically, 0.05 g of photocatalyst loaded with Pt (1 wt.%) was dispersed by magnetic stirrer in 80 mL of aqueous solution containing 0.5 M Na_2S and 0.5 M Na_2SO_3 . Prior to irradiation, the suspension of catalyst was dispersed by an ultrasonic bath for 10 min, and then purged with nitrogen for 20 min to completely remove the dissolved oxygen and ensure the reactor was in an anaerobic condition. A 0.4 mL gas was intermittently sampled through the septum, and the amount of H_2 was determined by gas chromatography (GC-14C, Shimadzu, Japan, TCD, with nitrogen as a carrier gas and 5 Å molecular sieve column).

The photocatalytic performances of g-CS@TiO_{2-x} were also evaluated via the degradation of four kinds of pollutants, like RhB, MB, CIP, and 4-CP under visible light irradiation in an open home-made thermostatic photoreactor. Before light irradiation, a suspension containing 80 mL of 10 mg/L pollutants solution and 80 mg of a solid catalyst was sonicated for 10 min and then stirred 1 h in the dark to ensure an adsorption–desorption equilibrium. Then the suspension was irradiated under continuous stirring by using a 350 W Xenon arc lamp with a UV-cutoff filter (420 nm) and was positioned 20 cm away from the reactor. At certain time intervals, 5 mL suspensions were sampled and centrifuged for subsequent measurement with a UV–vis spectrophotometer (UV-2450, Shimadzu). To establish the stability of the photocatalysts, the used photocatalyst was recycled for testing subsequent photocatalytic activities as follows. After a photocatalytic experiment, the composite was recovered by washing with distilled water three times, drying at 80°C for 24 h.

To detect the active species generated in the photocatalytic system, various scavengers, including *tert*-butanol (*t*-BuOH), ammonium oxalate (AO) and 1,4-benzoquinone (BQ), were introduced into the solution of RhB. *t*-BuOH, AO, and BQ were used as the hydroxyl radical ($\cdot\text{OH}$) scavenger, hole (h^+) scavenger, and superoxide radical ($\text{O}_2^{\cdot-}$) scavengers, respectively.

3. Results and discussion

3.1. DFT calculation results

First-principles calculation based on DFT were used to study the electronic structures of TiO_2 , TiO_{2-x} , and g-CS@TiO_{2-x} . The supercells of these three photocatalysts were built, and the optimized structures are shown in Fig. 1. Fig. 1A shows the supercell of pristine TiO_2 nanocrystals without Ti^{3+} but with fully relaxed surface dangling bonds. The red balls stand for oxygen atom and purple for titanium atom. Fig. 1D gives the total (TDOS) and partial DOS (PDOS) of pristine TiO_2 . As can be observed from Fig. 1D, the valence and conduction states are mainly derived from the O 2p orbitals and the Ti 3d orbitals, respectively. We further established partial reduced TiO_2 (TiO_{2-x}) model by removing lattice oxygen atom between two interstitial voids (Fig. 1B), and TDOS and PDOS of TiO_{2-x} are obtained (Fig. 1E). It can be observed from TDOS in Fig. 1E that a small energy level near the conduction band minimum (CBM) is generated after introducing Ti^{3+} state, accompanied by a reduced band gap. Moreover, as shown in the PDOS of TiO_{2-x} , this small energy level formed is derived from Ti 3d orbitals, which mainly ascribed to the existence of Ti^{3+} . The g-CS@TiO_{2-x} structure is also constructed (Fig. 1C). After the combination of TiO_{2-x} with g-CS,

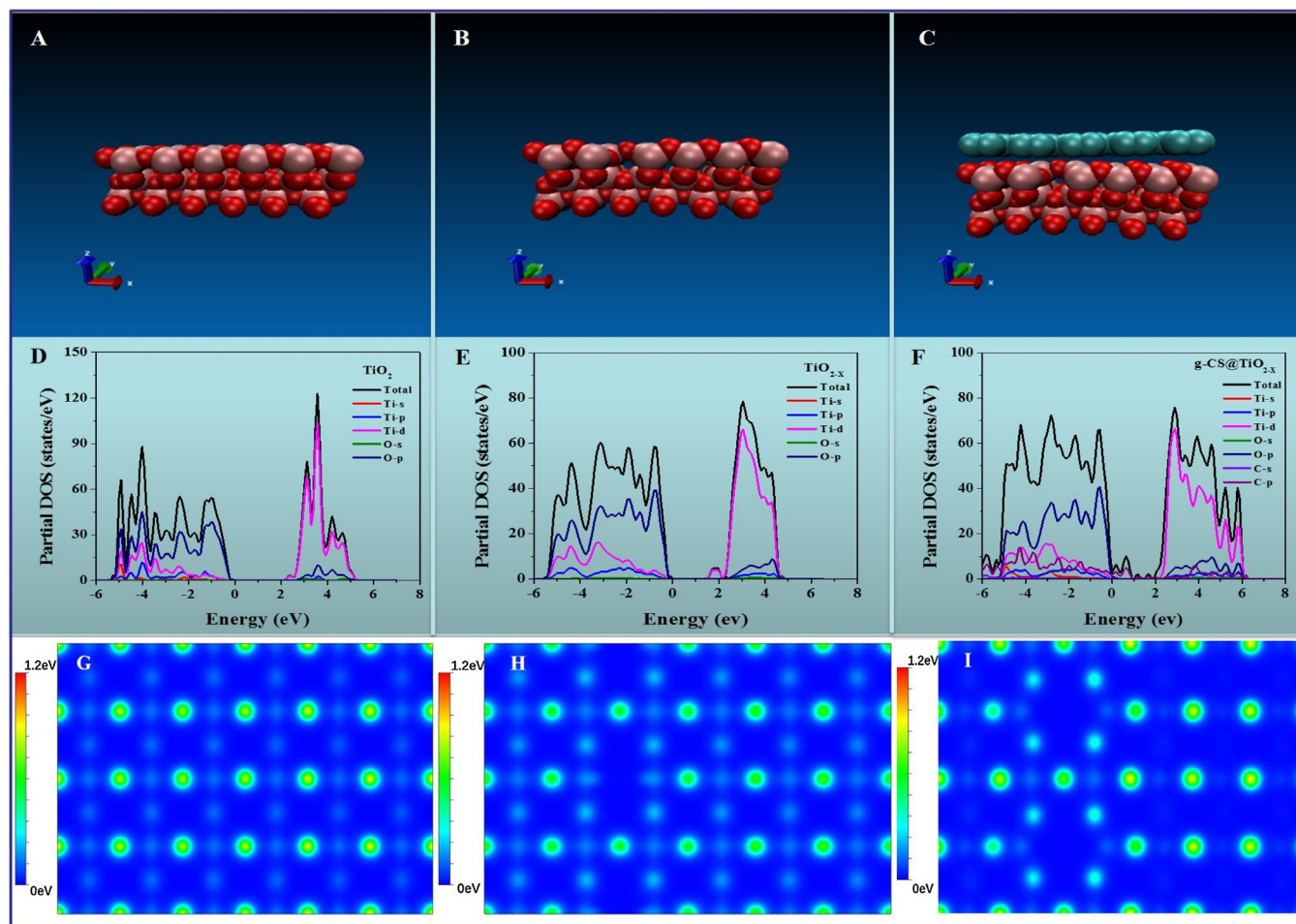


Fig. 1. Calculated models, partial density of states (PDOS) and charge density difference for TiO_2 (A, D and G), TiO_{2-x} (B, E and H), and g-CS@TiO_{2-x} (C, F and I).

some mid-gap states localized between the valence band maximum (VBM) and conduction band minimum (CBM) can be discerned in the DOS of g-CS@TiO_{2-x} composite. The nature of these mid-gap states is investigated by the calculated PDOS (Fig. 1F). As can be seen from Fig. 1F, the mid-gap states formed are mainly derived from the C 2p orbitals. These newly formed mid-gap states can further reduce the bandgap of g-CS@TiO_{2-x} . In this case, when the composite of g-CS@TiO_{2-x} is irradiated under visible light, the electrons excited can transfer from VB of TiO_{2-x} to these mid-levels or from one mid-level to CB of TiO_{2-x} easily, meanwhile, the generated electrons in the CB of TiO_{2-x} are more difficult to move back from CB to VB, which prevents the corresponding recombination more efficiently [39–41]. The charge densities of as-prepared samples were further investigated. In contrast to normal TiO_2 , the O and Ti atoms of TiO_{2-x} and g-CS@TiO_{2-x} get less electrons (Fig. 1G–I), which further proved that Ti^{3+}/O vacancies exist in the lattice of TiO_{2-x} and g-CS@TiO_{2-x} .

To gain insight into the interface property of g-CS@TiO_{2-x} , the binding energy is calculated. The binding energy of g-CS on the surface of TiO_{2-x} is calculated by subtracting the energies of the bare slab and the free molecule from the total energy of the slab plus the adsorbed molecule as shown in equation: $\text{BE} = E_{(\text{ads/slab})} - E_{\text{slab}} - E_{\text{molecule}}$, where $E_{(\text{ads/slab})}$, E_{slab} and E_{molecule} are the total energy of the relaxed g-CS@TiO_{2-x} , the TiO_{2-x} and the bare g-CS layer, respectively [42,43]. All these models are calculated under the same calculation condition to ensure the consistency of our calculation. The binding energy of g-CS@TiO_{2-x} is calculated to be -12.2 eV , according to the above-mentioned equation, which indicated that

charge interaction may occur in the g-CS@TiO_{2-x} interface. In addition, according to the previous reports, the carbon materials can be acted as electron acceptors [44,45], which are beneficial to the separation of photo-excited carriers, and thus improve the photocatalytic activity of as-prepared composites. In this case, thanks to the strong interaction effect between carbon atom and TiO_2 , some new C–O bonds could be formed due to the binding between the free electrons on the surface of TiO_{2-x} with some unpaired π -electrons, which also be proved by the previous carbon- TiO_2 system [39,46]. These newly formed bonds are further investigated by XPS spectra.

4. Morphology and structure properties

4.1. TEM and SEM analysis

The transmission electron microscopy (TEM) and scanning electron microscopy (SEM) images of the g-CS@TiO_{2-x} as well as g-CS showed large-scale monodispersed spheres with a uniform size of ca. $1 \mu\text{m}$ (Fig. 2A and D). The high magnification SEM and TEM images of selected individual single particle (Fig. 2B,C,E and F) clearly disclose that small TiO_2 nanodots with size of about 5 nm are uniformly and well dispersed on the surface of g-CS. Moreover, TEM images (Fig. 2G) of the as-prepared g-CS@TiO_{2-x} microspheres obtained from Fig. 2F also clearly showed that the surface is evenly covered by TiO_2 nanodots, which is mainly driven by organic groups on the surface of the carbon spheres (Fig. S1-FTIR). The microstructure of the TiO_2 nanodots on the surface of g-CS@TiO_{2-x}

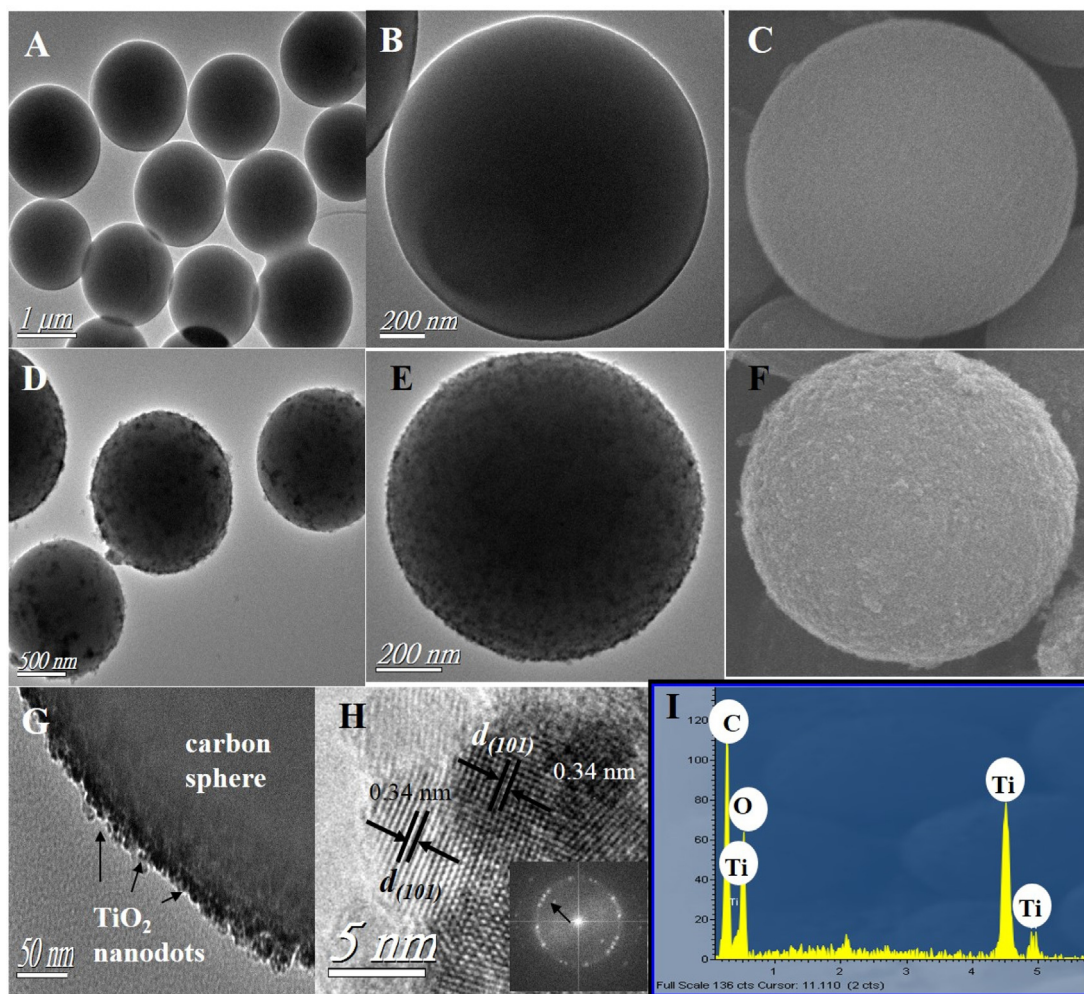


Fig. 2. TEM/SEM images of g-CS (A–C, G) and g-CS@TiO_{2-x} (D–F) microspheres; HRTEM images of g-CS@TiO_{2-x} microspheres (H), inset (H) is the FFT image recorded on HRTEM image of H; EDS image of g-CS@TiO_{2-x} microspheres (I).

microspheres is further clearly observed by the high-resolution TEM (HRTEM) image (Fig. 2H). The HRTEM image (Fig. 2H) obtained from Fig. 2G shows that fringe lines with 0.34 nm spacing are for the corresponding (101) facet of anatase TiO₂ (inset is FFT, which also shows diffraction ring of (101)). Bare TiO₂ nanoparticles suffered serious aggregation, as shown in Fig. S2. After incorporating of g-CS, TiO₂ nanodots are well dispersed on a whole g-CS. Therefore, g-CS plays a crucial role in the construction of g-CS@TiO_{2-x} microspheres, which can greatly enhance the dispersion of TiO₂ NPs. Moreover, The EDS spectrum in Fig. 2I also clearly indicates that the composite consists C, O and Ti elements.

4.2. XRD and Raman analysis

X-ray diffraction measurements (XRD) are performed to identify the crystalline phase and the structure. The XRD patterns of TiO₂, TiO_{2-x}, g-CS@TiO_{2-x} and the mechanical mixture of g-CS and TiO_{2-x} (g-CS + TiO_{2-x}) are shown in Fig. 3A and B. All of the as-prepared samples exhibit good crystallinity. For TiO₂, the diffraction peaks with 2θ values of 25.2°, 37.8°, 47.9°, 53.9°, 54.9°, 62.6°, 68.8° and 74.9° correspond to the (101), (004), (200), (105), (211), (204) and (220) crystal faces of anatase TiO₂, respectively, which are consistent with the values in the standard card (JCPDS no. 21-1272; a = 3.785 Å and c = 9.513 Å), and no impurities are detected [47]. For TiO_{2-x}, g-CS@TiO_{2-x}, and g-CS + TiO_{2-x}, similar peaks could be observed. Nevertheless, it is noted that the characteristic peak (101)

Table 1

Lattice constants of TiO₂ and partial reduced TiO₂ (TiO_{2-x}).

sample	a (Å)	b (Å)	c (Å)
26-1272 ^a	3.785	3.785	9.514
TiO ₂ ^b	3.786	3.786	9.512
TiO _{2-x} ^b	3.789	3.789	9.473
Ti ₃₂ O ₆₄ ^c	3.695	3.687	9.589
Ti ₃₂ O ₆₃ ^c	3.729	3.703	9.393

^a Standard JCPDS card of anatase TiO₂.

^b Calculated from XRD pattern.

^c Cluster calculated using DFT.

of all these three samples are slightly shifted to lower 2θ values compared to pristine TiO₂, suggesting that the lattice constants are changed. This tiny change could be attributed to the presence of Ti³⁺/oxygen vacancies [48]. In addition, the lattice constants of as-prepared pristine TiO₂ and TiO_{2-x} were calculated from XRD patterns. As can be observed from Table 1, the c axis of TiO_{2-x} is shortened, whereas the a and b axes are elongated compared with pristine TiO₂. Meanwhile, DFT calculations on the cell structure were also investigated. Calculation results indicated that the c axis shrinks heavily in the presence of Ti³⁺, whereas the a and b axes just enlarge in small increments, which is consistent with XRD calculation results [48].

Fig. 3C shows the Raman spectra of as-prepared samples. The as-prepared pristine TiO₂ shows four obvious peaks located at

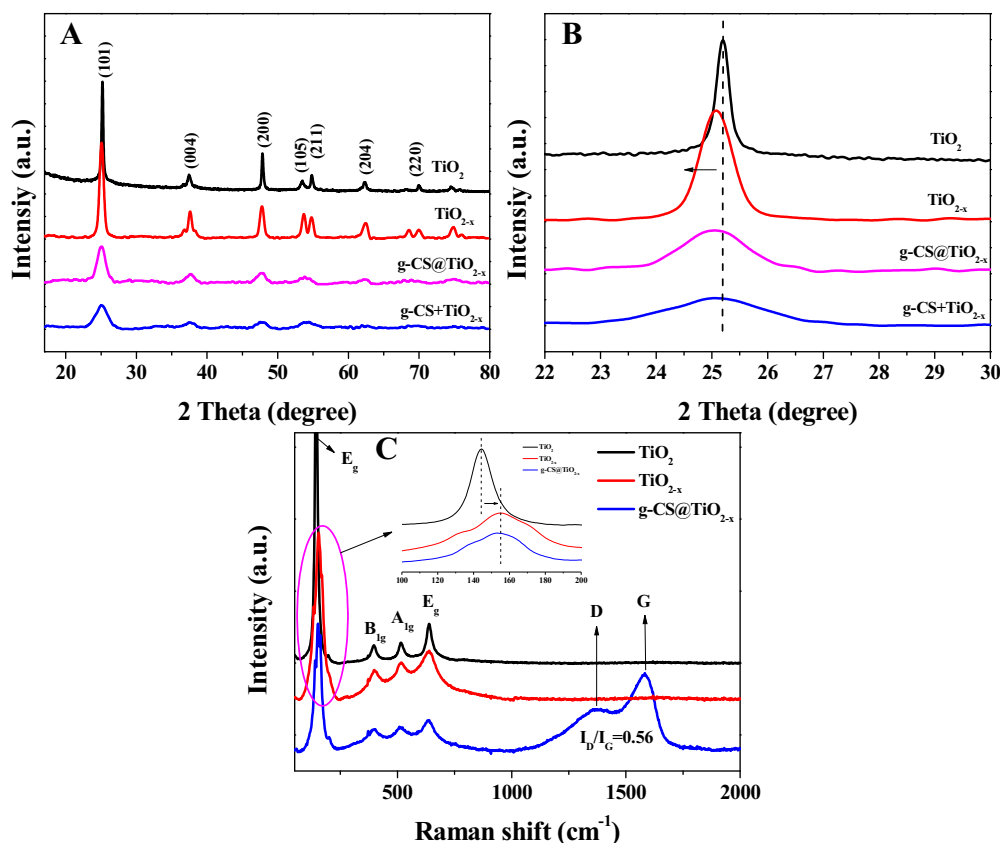


Fig. 3. XRD patterns (A and B) of TiO_2 , TiO_{2-x} , g-CS@TiO_{2-x} , and g-CS+TiO_{2-x} ; Raman spectra (C) of TiO_2 , TiO_{2-x} and g-CS@TiO_{2-x} (inset is enlarged Raman spectra).

146 (E_g), 399 (B_{1g}), 516 (A_{1g}), and 640 cm^{-1} (E_g), which can be attributed to the characteristic peaks of the anatase phase. However, from the enlarged view of the Raman spectra, we can find that the peak of E_g in the samples of TiO_{2-x} and g-CS@TiO_{2-x} are red-shift compared with pristine TiO_2 , which is consistent with previous reports (the Ti^{3+} /oxygen vacancies will lead to the red-shift of Raman E_g vibration) [49]. Additionally, the broadening band width of E_g in both TiO_{2-x} and g-CS@TiO_{2-x} further proved the existence of Ti^{3+} /oxygen vacancies [50]. Two characteristic peaks of g-CS@TiO_{2-x} were observed at approximately 1367 cm^{-1} and 1583 cm^{-1} , which are attributed to the disorder-induced D band and G band. This result proved the presence of carbon spheres in the composites (the carbon peaks were not shown in the XRD). In general, the D band is attributed to the vibrations of carbon atoms with dangling bonds in disordered graphite planes and the defects incorporated into graphite-like structures [51], and the G-band is attributable to the first order scattering of the E_{2g} phonon of sp^2 C atoms [52]. The intensity ratio of the D and G bands (I_D/I_G) had been estimated to be around 0.56, which suggested that TiO_2 nanodots were deposited on the surface of sp^2 -bonded carbon, helping the improvement of the g-CS@TiO_{2-x} conductivity, and prompting the transmission and separation of photogenerated carriers.

5. Chemical states analysis

5.1. XPS and ESR analysis

The surface chemical compositions and chemical states of the resultant crystal are investigated by means of XPS. Fig. 4A–C shows the XPS spectra of Ti 2p, O 1s, and C 1s for the as-synthesized TiO_2 and g-CS@TiO_{2-x} . As shown in Fig. 4A, two peaks of TiO_2 at 458.8 and

464.5 eV are corresponded to the Ti 2p_{3/2} and Ti 2p_{1/2} spin-orbital splitting photoelectrons in Ti^{4+} chemical state, respectively [53]. As for g-CS@TiO_{2-x} (Fig. 4A), these two peaks slightly shift to a lower bonding energy (458.6 and 464.3 eV), which can be ascribed to the formation of Ti^{3+} on the surface of as-prepared hybrid according to the previous report [53]. The peak fitting result of Ti_{2p} spectrum is provided (Fig. S3). As can be observed from Fig. S3, the peak located at ca. 457.8 eV is attributed to Ti^{3+} . The detailed quantitative results for Ti^{3+} in the composite were obtained by two clear fitting peaks including Ti^{4+} and Ti^{3+} . The Ti^{4+} : Ti^{3+} peak area ratio is about 6.4: 1, suggesting the Ti^{3+} is about 13.5% within the composite. The presence of Ti^{3+} center is further confirmed by electron spin resonance (ESR). The as-prepared TiO_{2-x} and g-CS@TiO_{2-x} samples both gave rise to a strong ESR signal, while no signal is observed for pristine TiO_2 (Fig. 4D). The ESR spectra of TiO_{2-x} and g-CS@TiO_{2-x} show intense signal located at the g of 2.003, which further indicates that unpaired spins of $\text{Ti}^{3+} 3d^1$ existed in as-prepared photocatalysts [54]. Additionally, to test stability of as-prepared g-CS@TiO_{2-x} , ESR analysis is performed after the g-CS@TiO_{2-x} was synthesized for six months, and the results indicates that high stable reduced TiO_2 composites were obtained (the intensity of ESR peak do not decrease) through this simple, gentle and green strategy. Fig. 4B demonstrates that the O 1s peak of TiO_2 around 529.9 is assigned to the Ti–O bonds in the TiO_2 lattice [55]. In contrast to the pure TiO_2 NPs, g-CS@TiO_{2-x} has a binding energy shift toward high energy by 0.1 eV for O (530.0 eV), which may be caused by the extra electrons from oxygen defects in the TiO_2 crystal lattice (band bending effect). Fig. 4C shows the core level spectra of C1s for pristine TiO_2 and g-CS@TiO_{2-x} . The peak located at binding energy of 284.8 eV, corresponding to the C–C coordination, is observed for both of pristine TiO_2 and g-CS@TiO_{2-x} . Additionally, in g-CS@TiO_{2-x} , another peak

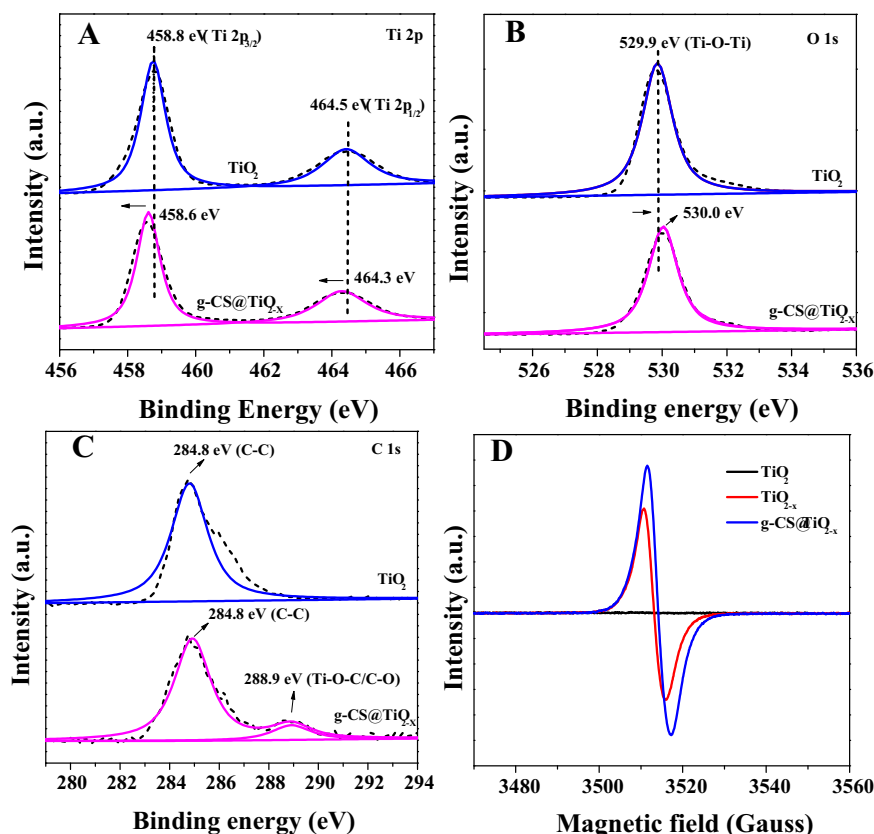


Fig. 4. XPS spectra of Ti 2p, O 1s and C 1s for the as-synthesized g-CS@TiO_{2-x}; ESR spectra of TiO₂, TiO_{2-x}, g-CS@TiO_{2-x}, and g-CS + TiO_{2-x}.

at 288.9 is observed, which could be because of the formation of Ti—O—C structure reported by many research groups [56,57]. These results are consistent with DFT calculation results.

5.2. Band structure analysis

Considering that the visible-light absorption property played an important role in determining the visible-light photocatalytic activity of photocatalysts, the UV–vis diffused reflection spectra (DRS) studies are performed. Fig. 5A shows the DRS of the as-prepared samples, which reflect the optical properties and different band gap structure of the as-prepared photocatalysts. Pure TiO₂ absorbs only ultraviolet light with its fundamental absorption edge near 400 nm. Compared with pristine TiO₂, the TiO_{2-x} shows improved absorption in the region between 400 and 800 nm. Meanwhile, the absorption edge of TiO_{2-x} exhibits an obvious red shift relative to pristine TiO₂, suggesting that the band gap of partial reduced TiO₂ is narrowed. We further evaluate the DRS of g-CS@TiO_{2-x}. As expected, the absorption intensity from 400 to 800 nm further enhanced. The spectrum of g-CS + TiO_{2-x} is investigated as a reference profile. In order to compare the photovoltaic performance of partial reduced TiO₂ and g-CS@TiO_{2-x} to that pristine TiO₂, incident photon to current conversion efficiency (IPCE) spectra of these three photocatalysts were collected [58]. As can be observed from Fig. 5B, the TiO₂ and g-CS@TiO_{2-x} possessed higher IPCE values over a wide range than pristine TiO₂, which was consistent with the UV–vis DRS results. The band gap energies are calculated from the extrapolation of the absorption edges and the equation $E_g = 1240/\lambda$. The band gap energies of the pristine TiO₂, TiO_{2-x}, g-CS + TiO_{2-x}, and g-CS@TiO_{2-x} were calculated to be about 3.1, 2.6, 2.5, and 2.3 eV. This result is consistent with the DFT calculation result. In a word, TiO_{2-x}, g-CS + TiO_{2-x}, and g-CS@TiO_{2-x}

composites are able to be photoexcited by visible light irradiation, by which photocatalytic reactions could be performed. The VBM of TiO₂ and g-CS@TiO_{2-x} are measured to be 2.4 and 1.7 eV by XPS valence spectra, as shown in Fig. 5C. Combining the DRS results with the formula of $E_{CB} = E_{VB} - E_g$, the CBM position can be calculated to be −0.7 eV for TiO₂ and −0.6 eV for g-CS@TiO_{2-x}. Based on the above analysis, the energy band structure of g-CS@TiO_{2-x} can be obtained, as shown in Fig. 5D. The narrowing band gap could be ascribed to the existence of Ti³⁺ and g-CS.

5.3. PL analysis

The photoluminescence (PL) spectra are used to investigate the behavior of photo-generated electrons–holes pairs since PL emission results from the recombination of electrons and holes [59]. Generally speaking, the faster the recombination occurs, the more intense the PL spectrum is. Fig. 6 shows the PL spectra of as-prepared TiO₂, TiO_{2-x}, and g-CS@TiO_{2-x} excited at 362 nm. The emission spectra are recorded in the range of 400–700 nm. Obviously, pristine TiO₂ shows the highest intensity of emission peak, whereas the emission intensity of TiO_{2-x} is lower than that of TiO₂, indicating that electrons–holes pairs recombination rate of TiO_{2-x} is much lower than that of TiO₂. Predictably, after coupling with g-CS, the PL intensity of the as-prepared g-CS@TiO_{2-x} significantly further decreased, indicating efficient interfacial electron transfer from the conduction band of TiO_{2-x} to g-CS, which acts as electron sinks and suppress the recombination of photoinduced carriers [60–62]. The recombination of electrons and holes in g-CS@TiO_{2-x} significantly decreases, which benefits the photocatalysis.

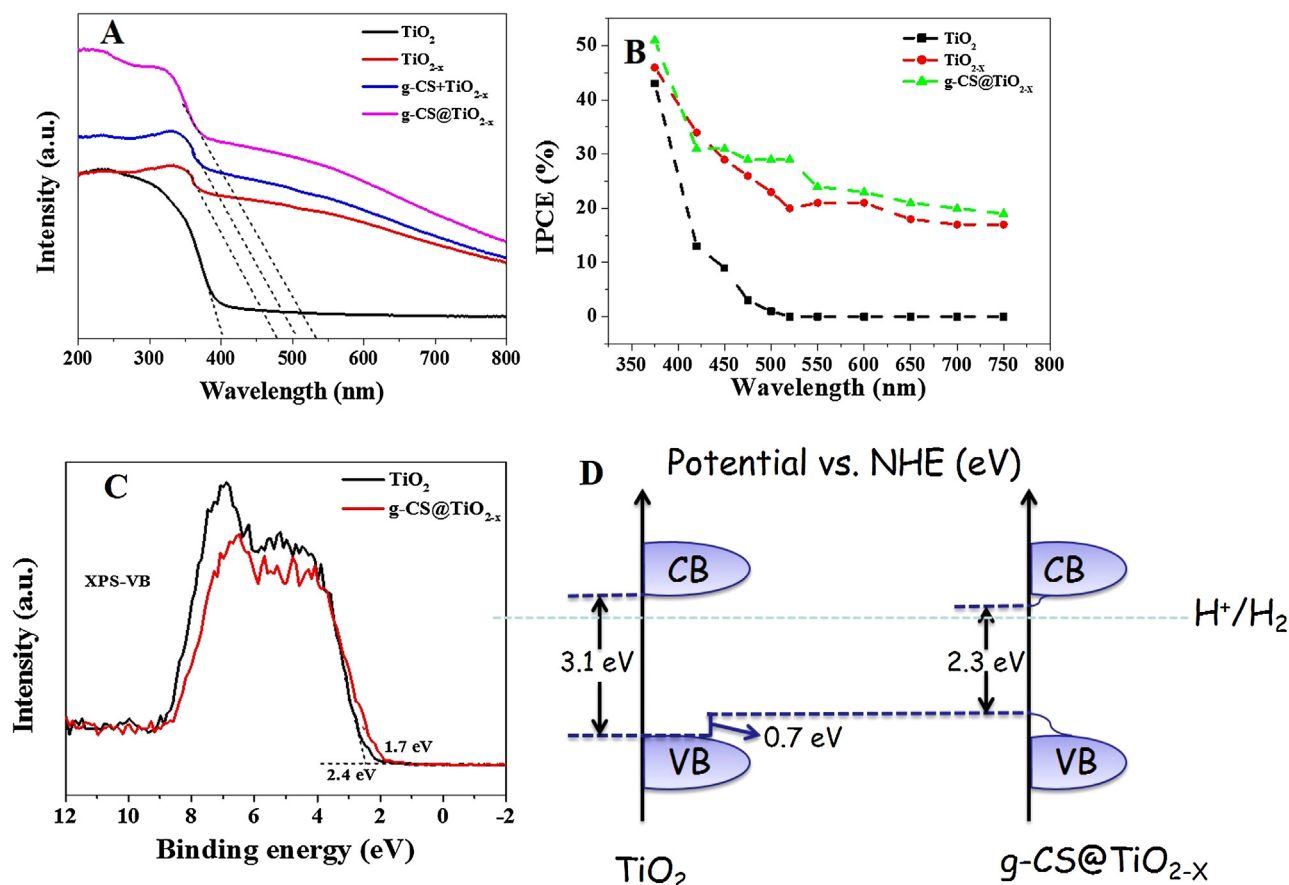


Fig. 5. UV-vis diffuse reflectance spectra (A), Incident photon to current conversion efficiency (IPCE) curves of the as-prepared photocatalysts (B), normalized XPS valence band spectra (C), and scheme for the energy band structure (D) of as-prepared samples.

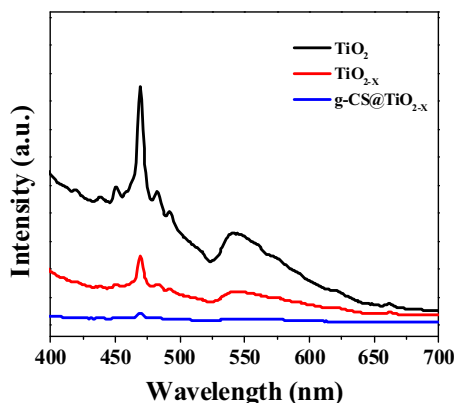


Fig. 6. PL spectra of TiO_2 , TiO_{2-x} , and g-CS@TiO_{2-x} .

5.4. Photoelectrochemical measurements

The photophysical behavior of the photoexcited charge carriers is further supported by transient photocurrent response of the samples in several on-off cycle tests under light irradiation. Photocurrent over time is detected on visible-light illumination at a bias potential of +0.1 V vs. SCE with the measured solution pH of 7.4. Fig. 7 compares the $I-t$ curves of TiO_2 , TiO_{2-x} , and g-CS@TiO_{2-x} and a good reproducibility of photocurrent is observed. The photocurrent increases sharply when the light is switched on, and immediately returns to its initial state after the light source is turned off, which

is repeatable [63,64]. This result demonstrated that most photo-generated electrons were transferred to the back contact across the samples to produce photocurrent under visible light irradiation [65]. Under illumination, the photocurrent intensity of TiO_{2-x} electrode is 3.5 times as high as that of pristine TiO_2 . The higher photocurrent density demonstrates more efficient charge separation and transportation in TiO_{2-x} , compared with pristine TiO_2 . In addition, the photocurrent value of TiO_{2-x} increased for about 1.8 times after combining with g-CS, indicating charge separation in the photo-electrochemical process had been promoted, confirming that more active catalytic sites and reaction centers could improve the photocatalytic activity. To further determine the advantage of g-CS@TiO_{2-x} over TiO_{2-x} and TiO_2 in improving the charge carriers transfer, electrochemical impedance spectra (EIS) Nyquist plots have also been performed. The EIS is conducted in 0.10 M KCl solution containing equimolar $[\text{Fe}(\text{CN})_6]^{3-/4-}$ at frequencies from 100 kHz to 0.1 Hz. Generally, the smaller radius of the Nyquist circle represents a lower charge-transfer resistance [66]. It can be seen from Fig. 7B that TiO_{2-x} shows smaller semicircle as compared to pristine TiO_2 , suggesting effective photogenerated electron-hole pairs separation achieved over the TiO_{2-x} electrode [67]. In addition, the g-CS@TiO_{2-x} sample shows the smallest semicircular arcs observed from the EIS spectra, indicating that a faster interfacial charge transfer to the electron acceptor occurs and results in an effective separation of electron-holes pairs after introducing of g-CS [68]. The results of photocurrent and EIS are consistent with the PL experimental results, which indicated that the formation of Ti^{3+} and the introduction of g-CS are the useful way to facilitate the effective

separation and transfer of the photogenerated electron–hole pairs. Thus, a better photocatalytic performance can be expected.

6. Photocatalytic performance

6.1. H_2 production performance

H_2 -production experiment is first carried out to investigate the accurate photocatalytic activity of as-prepared samples, as illustrated in Fig. 8. Before the photocatalytic experiment is performed, reference experiments are performed by taking 0.5 M Na_2S and 0.5 M Na_2SO_3 solution in the absence of either photocatalyst or irradiation. No appreciable amount of H_2 is detected, which suggests that H_2 is generated from the mixture solution of 0.5 M Na_2S and 0.5 M Na_2SO_3 by photocatalytic reaction on photocatalysts. The partial reduced TiO_2 (TiO_{2-x}) shows H_2 evolution rate (HER) of $46.9 \mu\text{mol h}^{-1} \text{g}^{-1}$ compared with pristine TiO_2 photocatalyst without activity under visible light (420 nm), which could be ascribed to the presence of Ti^{3+} . The HER of g-CS@ TiO_{2-x} is determined as $255.2 \mu\text{mol h}^{-1} \text{g}^{-1}$, 5.4 times higher than TiO_{2-x} , demonstrating that the addition of g-CS can enhance the HER performance of TiO_{2-x} . In addition, HER of the mechanical mixture of g-CS and TiO_{2-x} (g-CS + TiO_{2-x}) is determined to be $68.3 \mu\text{mol h}^{-1} \text{g}^{-1}$, which is lower than that of g-CS@ TiO_{2-x} . The enhanced HER of g-CS@ TiO_{2-x} should be attributed to its electronic property. In addition, the hydrogen production rate of g-CS@ TiO_{2-x} is also higher than those of many reported TiO_2 -based catalysts, which is summarized in Table S1. Moreover, it can be clearly found that no apparent deactivation of HER performances of the as-prepared photocatalysts during the second cycle are observed, while showing a similar trend to that in the first time, clearly indicating the good stability of as-prepared photocatalysts. The Quantum Efficiency (QE) was analysed at 420 nm, and the average light intensity is 60 mW. The QE of g-CS@ TiO_{2-x} was calculated to be 3.8% ($QE = 2n(H_2)/n(\text{incident photons})$), which is also higher than those of previous reports (Table S2).

The photocatalytic activities of g-CS@ TiO_{2-x} are further investigated by monitoring the decomposition of RhB and MB under visible light irradiation. According to the adsorption–desorption behavior results of photocatalysts without light irradiation, after 1 h adsorption, there was almost no change in the concentration of pollutions, which indicated that the adsorption–desorption behavior reached an equilibrium. Fig. 9A and C show the time-dependent concentration of dye using g-CS@ TiO_{2-x} composite as well as g-CS + TiO_{2-x} , TiO_{2-x} , and TiO_2 as photocatalysts under visible light irradiation. RhB and MB can only be slightly degraded (8%/5% for RhB/MB) under visible light irradiation without catalysts, suggesting that photolysis of RhB/MB is negligible. The photodegradation activities are similar to the H_2 evolution activity of as-prepared photocatalysts. TiO_2 could be degraded less than 45%/35% of the RhB/MB after 3 h/2 h of visible light irradiation due to this poor visible light absorption capability. After part of Ti^{4+} is reduced to Ti^{3+} , the visible-light degradation efficiency of TiO_{2-x} increases to be about 65%/64% (RhB/MB). Additionally, with the incorporation of g-CS to TiO_{2-x} , the photodegradation activity further improved greatly. We can clearly see the nearly complete degradation of RhB/MB for g-CS + TiO_{2-x} after visible irradiation for 3 h/2 h. Moreover, the mechanical mixture of g-CS and TiO_{2-x} is selected as a reference sample. The photocatalytic activity of g-CS@ TiO_{2-x} composite is also higher than that of g-CS + TiO_{2-x} . In order to investigate the photocatalytic activity of as-prepared samples thoroughly, the photocatalytic data are fitted based on the pseudo-first-order kinetic equation: $\ln(C/C_0) = -kt$, in which the value of rate constant k is equal to the corresponding slope of the fitting line. The linear relationship of $\ln(C/C_0)$ vs. time is

shown in Fig. 9B and D. The pseudo-first-order rate constants over TiO_2 , TiO_{2-x} , g-CS@ TiO_{2-x} , and g-CS + TiO_{2-x} are 0.0033/0.0034, 0.0057/0.0084, 0.012/0.0213, and 0.0064/0.011 min^{-1} for RhB/MB, respectively. Based on these results, one can see that g-CS@ TiO_{2-x} exhibits the highest photodegradation activity which is 3.6/6.3 (RhB/MB) times than that of pristine TiO_2 . In addition, the photodegradation activity of g-CS@ TiO_{2-x} is also higher than those of many reported TiO_2 -based photocatalysts. Comparison of the results is shown in the Supporting information (Tables S2 and S3).

Similar enhancement of photocatalytic activity is also found in degradation of other environmental pollutants. 4-CP, which is commonly found in wastewater from the paper, pharmaceutical, and dyestuff industries, is posing a serious risk to the environment [69]. CIP, a kind of antibiotics, is widely used for treating bacterial infections. Consequently, it is often found in aquatic environments, which may pose serious threat to the ecosystem and human health by inducing bacterial drug resistance [70]. Thus, these two pollutions are chosen to investigate the photocatalytic activity of as-prepared samples under visible-light irradiation, as shown in Fig. 9E. Composite of g-CS@ TiO_{2-x} still exhibits the highest photoactivity towards the degradation of 4-CP and CIP among the four as-prepared samples.

For practical applications in aqueous solution, the reusability and stability of g-CS@ TiO_{2-x} composite are very critical in the process of photocatalysis. To investigate the recyclability of photocatalyst, repetitive experiments have been conducted by centrifugation and reused in the next photocatalytic reaction for five times under the same conditions. As shown in Fig. 9F, the concentration of RhB after the first cycle was reduced by 98% after 3 h irradiation; while it is degraded about 94% at the fifth cycle under the same experimental condition. Obviously, the photocatalytic activity of the g-CS@ TiO_{2-x} composite remained almost unchanged. Therefore, the as-prepared g-CS@ TiO_{2-x} composite shows an excellent catalytic stability, performing as genuine heterogeneous visible-light-driven photocatalysts for the treatment of pollutions.

6.2. Free radicals/holes scavenging experiments and ESR analysis

The mobility of photo-excited carriers is important in the photocatalytic process, as it manages the subsequent production of reactive oxygen species (ROS) and the photocatalytic efficiency. To deeply understand the mechanism of enhanced photocatalytic activity of as-prepared g-CS@ TiO_{2-x} , the active species generated during the RhB degradation process are identified by free radical and hole trapping experiments using various scavengers including *t*-BuOH ($\cdot\text{OH}$ scavenger), AO (h^+ scavenger), and BQ ($O_2^{\cdot-}$ scavenger) [71]. As shown in Fig. 10A, after 1 mmol *t*-BuOH as a scavenger for $\cdot\text{OH}$ radical species is added, the degradation efficiency of RhB is not suppressed, indicating the absence of $\cdot\text{OH}$ radical species. Whereas the degradation rate over g-CS@ TiO_{2-x} sample is suppressed significantly in the presence of 1 mmol of BQ, suggesting that the active species of $O_2^{\cdot-}$ play an important role toward the degradation of RhB. Additionally, the addition of AO to the reaction system restrains the photocatalytic activity of g-CS@ TiO_{2-x} greatly. These results indicated that active species including h^+ and $O_2^{\cdot-}$ have played crucial roles during the process of RhB degradation in the g-CS@ TiO_{2-x} photocatalytic system under visible light irradiation. However, almost no $\cdot\text{OH}$ radicals were generated in the current photocatalytic system.

To further investigate the photocatalytic process, the electron spin resonance (ESR) technique is investigated because ESR can be applied to reveal the reactive free radicals in photocatalytic reaction systems [72]. The superoxide radicals ($O_2^{\cdot-}$) and hydroxyl radicals

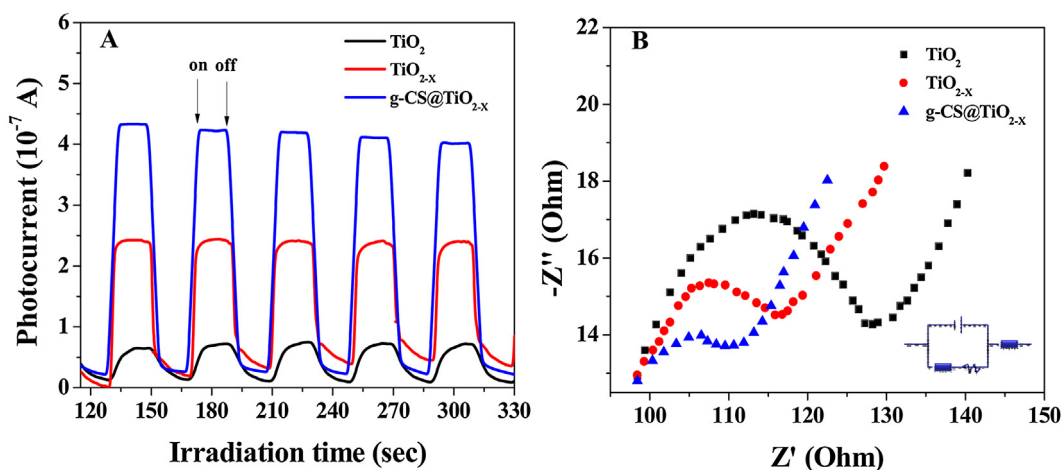


Fig. 7. Time-based photocurrent response (A) and Nyquist plots (B) of TiO_2 , TiO_{2-x} , and g-CS@TiO_{2-x} .

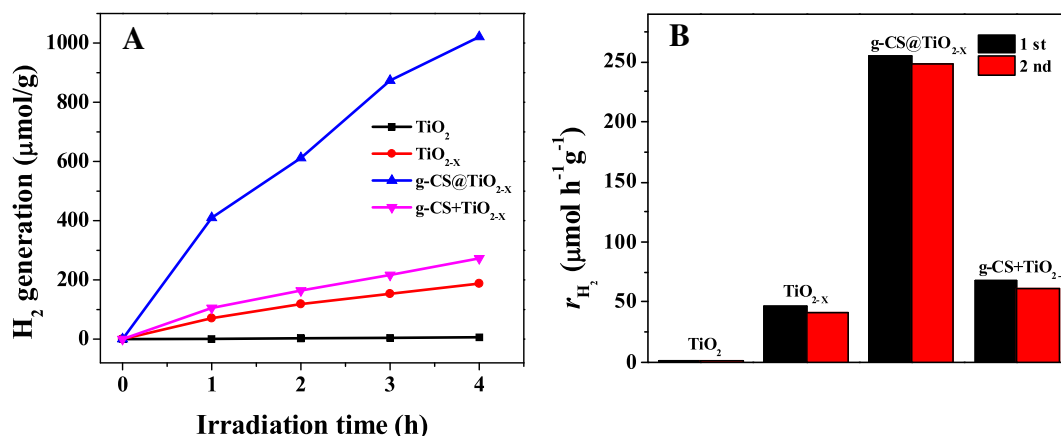


Fig. 8. Photocatalytic hydrogen evolution activity of as-prepared catalysts.

($\cdot\text{OH}$) are separately detected in methanol-medium and water-medium solutions on g-CS@TiO_{2-x} at room temperature in air. As shown in Fig. 10B, four characteristic peaks of $\text{DMPO-O}_2^{\cdot-}$ radical could be observed under visible light irradiation for 5 min, while no $\cdot\text{OH}$ signal is detected in dark under identical condition, which implying the $\text{O}_2^{\cdot-}$ radical are produced via single-electron reduction process. In addition, no $\text{DMPO}\cdot\text{OH}$ signal can be observed, indicating the $\cdot\text{OH}$ may be not the main active species during the photocatalysis process (Fig. 10C). Moreover, as observed in Fig. 5B, the VB value of g-CS@TiO_{2-x} (1.7 eV) is less positive than $E^0(\cdot\text{OH}/\text{OH}^-)$ (2.38 eV vs NHE), which suggesting that OH^- can't be oxidized to form $\cdot\text{OH}$ by holes of g-CS@TiO_{2-x} . However, the CB of g-CS@TiO_{2-x} (-0.6 eV) can reduce O_2 to produce $\text{O}_2^{\cdot-}$ radical because the $E^0(\cdot\text{OH}/\text{OH}^-)$ is only -0.046 eV. As a result, the ESR results and ROS trapping experiments are identical with the above-mentioned analysis.

6.3. Possible photocatalytic mechanism of the g-CS@TiO_{2-x} composites

Based on the above analysis, the possible photocatalytic mechanism diagram of the g-CS@TiO_{2-x} composites is obtained in Fig. 11. When the g-CS@TiO_{2-x} composite system is irradiated with visible light, electrons are excited from the VB to the CB and/or the mid-gap states of TiO_{2-x} , leaving electropositive holes at VB. Usually, these photo-excited carriers will quickly recombine and only

small amount of charges can participate in the photocatalytic process. However, in our system, the generated electrons in the CB of TiO_{2-x} are more difficult to move back to VB because of the formation of some mid-gap states between CB and VB of TiO_{2-x} , which prevents the corresponding recombination more efficiently. On the other hand, when g-CS is contact with TiO_{2-x} , the photogenerated electrons on the CB of TiO_{2-x} will further migrate to the surface of g-CS , which can also promote the separation of photo-generated electrons and holes. As a result, the enhanced visible light photocatalytic activity can be expected. This result is consistent with the results of DFT, PL, photocurrent, and EIS analysis. The accumulated electrons on the surface of g-CS are capable of reducing H^+ (O_2) into H_2 ($\text{O}_2^{\cdot-}$), and the $\text{O}_2^{\cdot-}$ species are responsible for the degradation and mineralization of pollutant in aqueous solution. Meanwhile, the corresponding photo-excited holes on the VB of TiO_{2-x} can subsequently oxidize the electron donor (D) and degrade pollutant directly.

In summary, the excellent visible light photocatalytic activity of the g-CS@TiO_{2-x} composites could be ascribed to the following reasons.

- (1) The presence of Ti^{3+} on the surface of g-CS@TiO_{2-x} composite can be responsible for the visible-light absorption because the impurity level induced by Ti^{3+} self-doping exists below the CBM of TiO_2 . This impurity level formed in the band gap of TiO_2 can reduce the energy gap of TiO_2 .

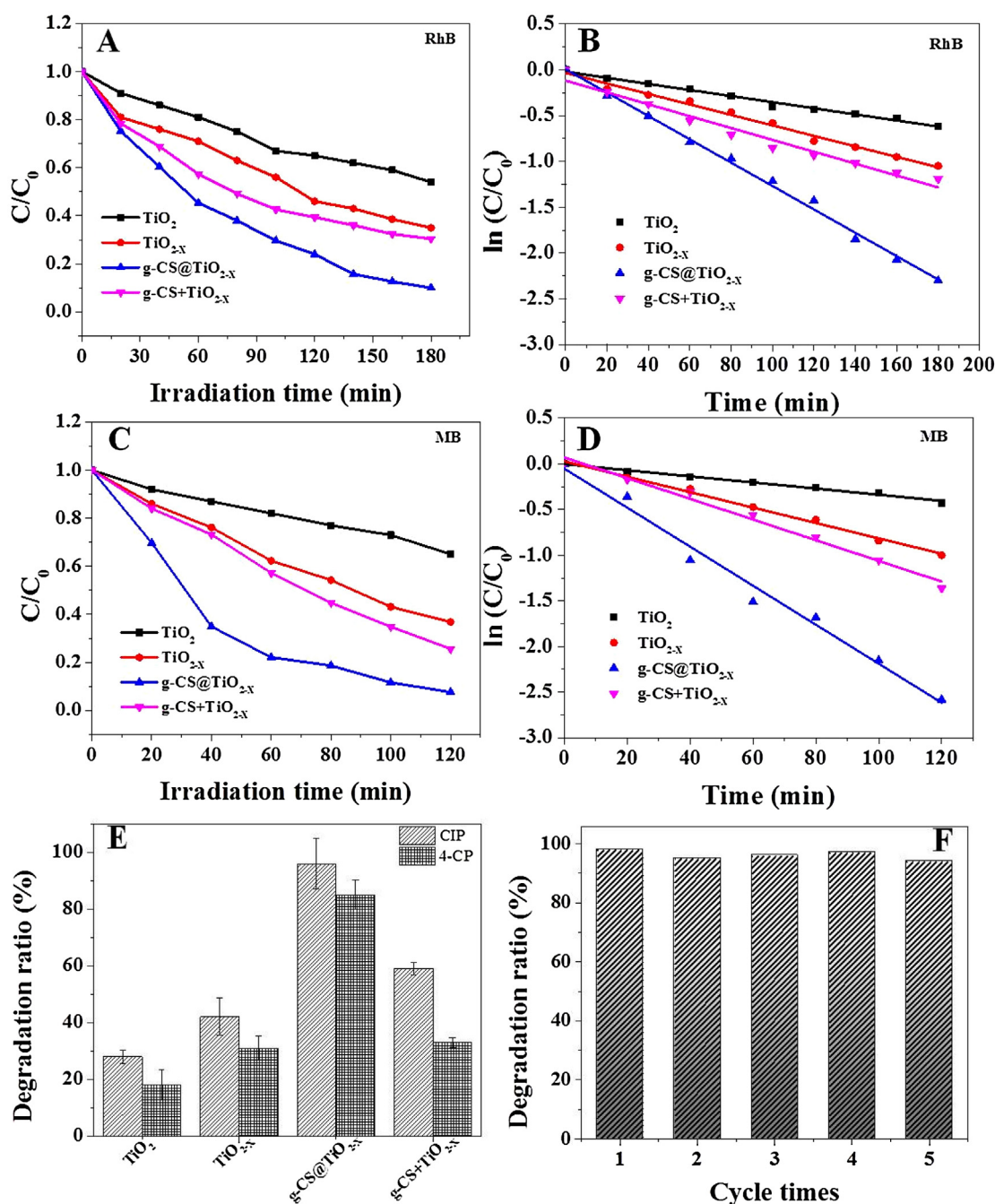


Fig. 9. Photocatalytic activity towards the degradation of RhB (A and B), MB (C and D), and CIP/4-CP (E); the possibility of recycling of the obtained g-CS@TiO_{2-x} photocatalyst (F).

- (2) g-CS acts as the electron acceptor in the g-CS@TiO_{2-x} system, promoting the charge separation and leaving more holes to form reactive species that promote the photocatalytic activity. On the other hand, according to the DFT and XPS results, connection bridge of Ti–O–C makes the two components highly electronically coupled. Additionally, the presence of g-CS can enhance the visible-light absorption, which may lead to the improvement of as-prepared photocatalyst.
- (3) The mid-gap energy levels are formed between the VBM and CBM of TiO₂ due to the introduction of g-CS, resulting in the electron transfer from VBM to a mid-gap energy level or from a mid-gap energy level to CBM more easily. In this way, the

electrons are more difficult to move back from CB to VBM, which prevents the corresponding recombination more efficiently.

7. Conclusion

In summary, we have successfully constructed a visible light active multifunctional composite g-CS@TiO_{2-x} via a mild solvothermal approach. The presence of reduced TiO₂ and g-CS not only significantly enhanced the visible-light photo-absorption but also introduced some isolated energy levels localized between the VBM and CBM. Moreover, the interfacial transfer of photogenerated elec-

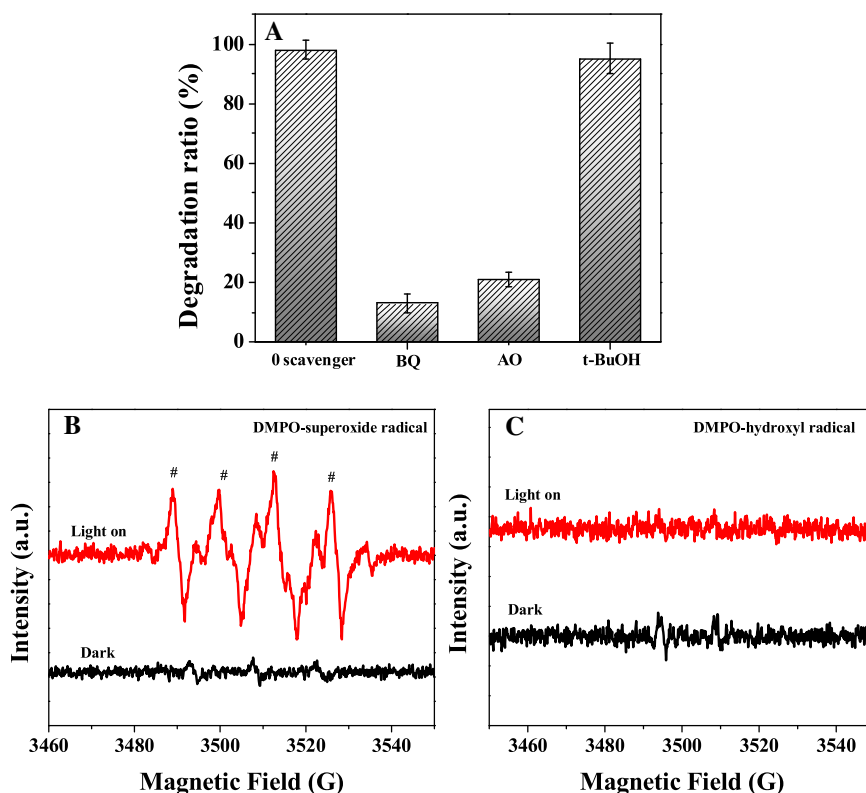


Fig. 10. The influence of various scavengers on the visible-light photocatalytic activity of g-CS@TiO_{2-x} towards the degradation of RhB (A); ESR spectra of radical adducts trapped by DMPO in g-CS@TiO_{2-x} hybrid materials aqueous dispersion under visible light irradiation.

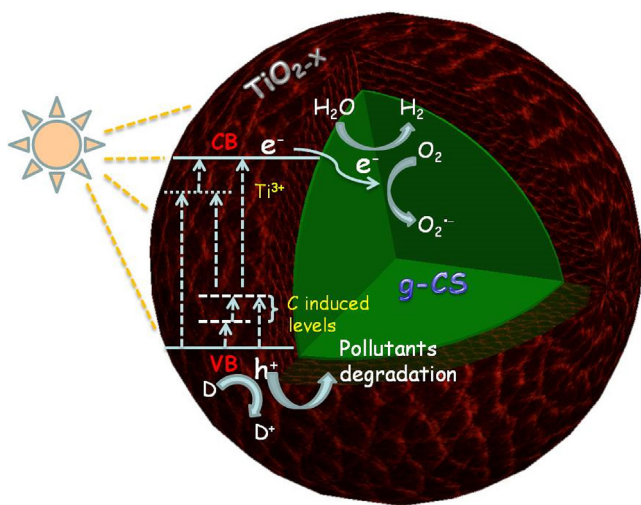


Fig. 11. Scheme of possible reaction mechanism of photocatalytic procedure.

trons between TiO_{2-x} and g-CS can lead to the effective charge separation. All these discoveries are investigated by DFT calculation, PL and photoelectrochemical measurements, and photocatalytic performance experiments. Based on the experimental results, the possible photocatalytic mechanism and photostability of the as-prepared composites were also investigated. Our work present here, can bridge the understanding of theory (DFT) and practical use (potential for efficient hydrogen generation and water cleaning) in building TiO₂-based catalysts.

Acknowledgements

The authors gratefully acknowledged the National Natural Science Foundation (21406091, 51402130, 21607063, 21676129), Hong Kong Scholar Program (XJ2016034), China Scholarship Council (201508320218), China Postdoctoral Science Foundation (2016M590421), China. The DFT calculations were performed using computational resources at the Center for Functional Nanomaterials, a user facility at BNL, supported by US Department of Energy.

Appendix A. Supplementary data

Supplementary data associated with this article can be found, in the online version, at <http://dx.doi.org/10.1016/j.apcatb.2016.11.044>.

References

- [1] A. Kubacka, M. Fernández-García, G. Colón, *Chem. Rev.* 112 (2012) 1555.
- [2] C. Yu, G. Li, S. Kumar, K. Yang, R. Jin, *Adv. Mater.* 26 (2014) 892.
- [3] R. Asahi, T. Morikawa, T. Ohwaki, K. Aoki, Y. Taga, *Science* 293 (2001) 269.
- [4] J. Pan, G. Han, R. Zhou, S. Zhao, *Chem. Commun.* 47 (2011) 6942.
- [5] N. Yang, Y. Liu, H. Wen, Z. Tang, H. Zhao, Y. Li, D. Wang, *ACS Nano* 7 (2013) 1504.
- [6] Z. Zheng, B. Huang, J. Lu, Z. Wang, X. Qin, X. Zhang, Y. Dai, M. Whangbo, *Chem. Commun.* 48 (2012) 5733.
- [7] K. Sasan, F. Zuo, Y. Wang, P. Feng, *Nanoscale* 7 (2015) 13369.
- [8] F. Zuo, L. Wang, T. Wu, Z. Zhang, D. Borchardt, P. Feng, *J. Am. Chem. Soc.* 132 (2010) 11856.
- [9] X. Chen, L. Liu, P. Yu, S. Mao, *Science* 331 (2011) 746.
- [10] G. Liu, L. Yin, J. Wang, P. Niu, C. Zhen, Y. Xie, H. Cheng, *Energy Environ. Sci.* 5 (2012) 9603.
- [11] T.R. Gordon, M. Cargnello, T. Paik, F. Mangolini, R.T. Weber, P. Fornasiero, C.B. Murray, *J. Am. Chem. Soc.* 134 (2012) 6751.
- [12] Y. Wang, C. Feng, M. Zhang, J. Yang, Z. Zhang, *Appl. Catal. B* 104 (2011) 268.
- [13] A. Naldoni, M. Allieta, S. Santangelo, M. Marelli, F. Fabbri, S. Cappelli, C. Bianchi, R. Psaro, V. Dal Santo, *J. Am. Chem. Soc.* 134 (2012) 7600.

- [14] Z. Wang, C. Yang, T. Lin, H. Yin, P. Chen, D. Wan, F. Xu, F. Huang, J. Lin, X. Xie, M. Jiang, *Energy Environ. Sci.* 6 (2013) 3007.
- [15] C. Yang, Z. Wang, T. Lin, H. Yin, X. Lu, D. Wan, T. Xu, C. Zheng, J. Lin, F. Huang, X. Xie, M. Jiang, *J. Am. Chem. Soc.* 135 (2013) 17831.
- [16] G. Wang, H. Wang, Y. Ling, Y. Tang, X. Yang, R. Fitzmorris, C. Wang, J. Zhang, Y. Li, *Nano Lett.* 11 (2011) 3026.
- [17] S. Hoang, S. Berglund, N. Hahn, A. Bard, C. Mullins, *J. Am. Chem. Soc.* 134 (2012) 3659.
- [18] A. Naldoni, M. Allietta, S. Santangelo, M. Marelli, F. Fabbri, S. Cappelli, C. Bianchi, R. Psaro, V. Santo, *J. Am. Chem. Soc.* 134 (2012) 7600.
- [19] F. Zuo, K. Bozhilov, R. Dillon, L. Wang, P. Smith, X. Zhao, C. Bardeen, P. Feng, *Angew. Chem. Int. Ed.* 51 (2012) 6223.
- [20] X. Lu, G. Wang, T. Zhai, M. Yu, J. Gan, Y. Tong, Y. Li, *Nano Lett.* 12 (2012) 1690.
- [21] M. Xing, W. Fang, M. Nasir, Y. Ma, J. Zhang, M. Anpo, *J. Catal.* 297 (2013) 236.
- [22] Z. Wang, C. Yang, T. Lin, H. Yin, P. Chen, D. Wan, F. Xu, F. Huang, J. Lin, X. Xie, M. Jiang, *Adv. Funct. Mater.* 23 (2013) 5444.
- [23] M. Wang, L. Sun, Z. Lin, J. Cai, K. Xie, C. Lin, *Energy Environ. Sci.* 6 (2013) 1211.
- [24] W. Zhou, Y. Leng, D. Hou, H. Li, L. Li, G. Li, H. Liu, S. Chen, *Nanoscale* 6 (2014) 4698.
- [25] L. Peng, T. Xie, Y. Lu, H. Fan, D. Wang, *Phys. Chem. Chem. Phys.* 12 (2010) 8033.
- [26] W. Teng, X. Li, Q. Zhao, G. Chen, *J. Mater. Chem. A* 1 (2013) 9060.
- [27] F. Su, T. Wang, R. Lv, J. Zhang, P. Zhang, J. Lu, J. Gong, *Nanoscale* 5 (2013) 9001.
- [28] Z. Cai, Z. Xiong, X. Lu, J. Teng, *J. Mater. Chem. A* 2 (2014) 545.
- [29] B. Rico-Ollera, A. Boudjemaab, H. Bahruji, M. Kebirb, S. Prashara, K. Bacharib, M. Fajardoa, S. Gómez-Ruiz, *Sci. Total Environ.* 563–564 (2016) 921.
- [30] H. Zhang, X. Lv, Y. Li, Y. Wang, J. Li, *ACS Nano* 4 (2009) 380.
- [31] K. Woan, G. Pyrgiotakis, W. Sigmund, *Adv. Mater.* 21 (2009) 2233.
- [32] Y. Yao, G. Li, S. Ciston, R. Lueptow, K. Gray, *Environ. Sci. Technol.* 42 (2008) 4952.
- [33] B. Tryba, A. Morawski, M. Inagaki, *Appl. Catal. B* 41 (2003) 427.
- [34] C. Silva, M. Sampaio, R. Marques, L. Ferreira, P. Tavares, A. Silva, J. Faria, *Appl. Catal. B* 178 (2015) 82.
- [35] H. Chun, W. Jo, *Appl. Catal. B* 180 (2016) 740.
- [36] Z. Lian, P. Xu, W. Wang, D. Zhang, S. Xiao, X. Li, G. Li, *ACS Appl. Mater. Interfaces* 7 (2015) 4533.
- [37] G. Kresse, J. Hafner, *Phys. Rev. B* 47 (1993) 558.
- [38] P. Blochl, *Phys. Rev. B* 50 (1994) 17953.
- [39] N. Yang, Y. Liu, H. Wen, Z. Tang, H. Zhao, Y. Li, D. Wang, *ACS Nano* 7 (2013) 1504.
- [40] G. Kresse, J. Hafner, *Phys. Rev. B* 47 (1993) 558.
- [41] G. Kresse, J. Furthmüller, *Phys. Rev. B* 54 (1996) 11169.
- [42] R. Lavanya, V. Surya, I. Lakshmi, K. Iyakutti, V. Vasu, H. Mizuseki, Y. Kawazoe, *Int. J. Hydrogen Energy* 39 (2014) 4973.
- [43] J. Graciani, Y. Ortega, J. Sanz, *Chem. Mater.* 21 (2009) 1431.
- [44] C. Han, Z. Chen, N. Zhang, J. Colmenares, Y. Xu, *Adv. Funct. Mater.* 25 (2015) 221.
- [45] W. Qian, P. Greaney, S. Fowler, S. Chiu, A. Goforth, J. Jiao, *ACS Sustain. Chem. Eng.* 2 (2014) 1802.
- [46] Y. Masuda, G. Giorgi, K. Yamashita, *Phys. Status Solidi B* 251 (2014) 1471.
- [47] Z. Jiang, W. Wei, D. Mao, C. Chen, Y. Shi, X. Lv, J. Xie, *Nanoscale* 7 (2015) 784.
- [48] B. Jiang, Y. Tang, Y. Qu, J. Wang Ying Xie, C. Tian, W. Zhou, H. Fu, *Nanoscale* 7 (2015) 5035.
- [49] X. Wang, J. Li, H. Kamiyama, M. Katada, N. Ohashi, Y. Moriyoshi, T. Ishigaki, *J. Am. Chem. Soc.* 127 (2005) 10982.
- [50] J. Wang, P. Yang, B. Huang, *Appl. Surf. Sci.* 356 (2015) 391.
- [51] G. Wang, J. Yang, J. Park, X. Gou, B. Wang, H. Liu, J. Yao, *J. Phys. Chem. C* 112 (2008) 8192.
- [52] H. Li, J. Liao, T. Zeng, *Catal. Sci. Technol.* 4 (2014) 681.
- [53] B. Jiang, C. Tian, Q. Pan, Z. Jiang, J. Wang, W. Yan, H. Fu, *J. Phys. Chem. C* 115 (2011) 23718.
- [54] Z. Wang, C. Yang, T. Lin, H. Yin, P. Chen, D. Wan, F. Xu, F. Huang, J. Lin, X. Xie, M. Jiang, *Energy Environ. Sci.* 6 (2013) 3007.
- [55] (a) Z. Jiang, C. Zhu, W. Wan, K. Qian, J. Xie, *J. Mater. Chem.* 4 (2016) 1806 (A); (b) Z. Jiang, D. Jiang, Z. Yan, D. Liu, K. Qian, J. Xie, *Appl. Catal. B: Environ.* 170 (2015) 195.
- [56] D. Gu, Y. Lu, B. Yang, Y. Hu, *Chem. Commun.* 2453 (2008).
- [57] J. Yu, G. Dai, Q. Xiang, M. Jaroniec, *J. Mater. Chem.* 21 (2011) 1049.
- [58] (a) Z. Hu, Z. Shen, J.C. Yu, *Chem. Mater.* 28 (2016) 564; (b) Z. Hu, G. Liu, X. Chen, Z. Shen, J.C. Yu, *Adv. Funct. Mater.* 26 (2016) 4445.
- [59] Q. Xiang, K. Lv, J. Yu, *Appl. Catal. B* 96 (2010) 557.
- [60] X. Bai, R. Zong, C. Li, D. Liu, Y. Liu, Y.F. Zhu, *Appl. Catal. B* 147 (2014) 82.
- [61] C. Pan, J. Xu, Y. Wang, D. Li, Y. Zhu, *Adv. Funct. Mater.* 22 (2012) 1518.
- [62] H. Li, J. Liu, W. Hou, N. Du, R. Zhang, X. Tao, *Appl. Catal. B* 160–161 (2014) 89.
- [63] Y. Bu, Z. Chen, W. Li, *Appl. Catal. B* 144 (2014) 622.
- [64] Y. Zhang, T. Mori, L. Niu, J. Ye, *Energy Environ. Sci.* 4 (2011) 4517.
- [65] H. Xu, J. Yan, Y. Xu, Y. Song, H. Li, J. Xia, C. Huang, H. Wan, *Appl. Catal. B* 129 (2013) 182.
- [66] Y. Zhang, N. Zhang, Z. Tang, Y. Xu, *ACS Sustain. Chem. Eng.* 1 (2013) 1258.
- [67] N. Zhang, M. Yang, Z. Tang, Y. Xu, *ACS Nano* 8 (2014) 623.
- [68] Y. Zhu, X. Ji, C. Pan, Q. Sun, W. Song, L. Fang, Q. Chen, C. Banks, *Energy Environ. Sci.* 6 (2013) 3665.
- [69] A. Nguyen, R. Juang, *J. Environ. Manage.* 147 (2015) 271.
- [70] Z. Jiang, X. Lv, D. Jiang, J. Xie, D. Mao, *J. Mater. Chem. A* 1 (2013) 14963.
- [71] S. Fang, Y. Xin, L. Ge, C. Han, P. Qiu, L. Wu, *Appl. Catal. B* 179 (2015) 458.
- [72] Y. Lv, Y. Zhu, J. Phys. Chem. C 117 (2013) 1852.